metals

MDPI

Article

Formation of the Structure and Properties of Deposited Multilayer Specimens from Austenitic Steel under Various Heat Removal Conditions

Dmitry A. Chinakhov [1,*] and Kirill O. Akimov [2]

[1] Institute of Metallurgy and Materials Science, Siberian State Industrial University, Novokuznetsk 654007, Russia
[2] Institute of Strength Physics and Materials Science SB RAS, Tomsk 634055, Russia
* Correspondence: chinakhov_da@mail.ru

Abstract: The effect of side limiters (shaping blocks) on the formation of the structure and hardness of AISI 308LSi stainless steel workpieces obtained by multilayer build-up welding in an argon environment has been studied. The studies were carried out on specimens deposited using graphite limiters, copper limiters and without limiters. As a result of numerical simulation, it was found that the lowest temperatures of the specimen metal are observed when using copper limiters, and the highest when using graphite limiters (different thermal conductivity of materials) in comparison with the temperatures of the specimen obtained without limiters. With the use of graphite limiters, most of the specimen's metal is in the temperature range of austenite formation (45%) and a more uniform growth of structural elements is observed, without sharp transitions between the deposited layers, in contrast to the other two types of specimens. The high value of the thermal conductivity of copper leads to an increase in the difference in the size of the dendrites between the central and peripheral side parts of the deposited specimen. The highest values of hardness are observed in the specimen obtained using graphite blocks, due to the more active diffusion of δ-ferrite into austenite by an average of 12%, compared with the other investigated specimens, despite the overall increase in size dendrites. The technology of electric arc multilayer build-up welding with the use of shaping graphite blocks makes it possible to produce a workpiece with a uniform structure and properties. The above makes it a promising direction in electric arc additive manufacturing.

Keywords: build-up welding; additive manufacturing; heat-transfer limiter; dendritic structure; hardness

Citation: Chinakhov, D.A.; Akimov, K.O. Formation of the Structure and Properties of Deposited Multilayer Specimens from Austenitic Steel under Various Heat Removal Conditions. *Metals* **2022**, *12*, 1527. https://doi.org/10.3390/met12091527

Academic Editor: Ricardo Branco

Received: 15 August 2022
Accepted: 13 September 2022
Published: 15 September 2022

1. Introduction

The development of new technologies for the manufacture of parts of a complex shape with desired structure and properties is one of the main tasks of modern manufacturing. Additive manufacturing technologies are one of the promising areas in solving the tasks due to their high rates of application and development [1]. The basis of additive manufacturing is the formation of metal layers in accordance with a previously prepared 3D model created by computer-aided design methods [2,3]. The automation and flexibility of such a production can reduce the time and cost of manufacturing complex geometries of a large number of parts [4,5]. It is possible to choose from several types of additive manufacturing in accordance with the International Standard ISO/ASTM 52900 [6]. For the production of metal parts, the technology of build-up welding powder materials [7–9] or wires [10–12] is used. The source of heating during the formation of the layer is a laser beam [7,8], an electron beam [7,9] or an electric arc [10–15].

The process of manufacturing parts from various powders by melting them with an electron or laser beam is widely used in additive technologies today. These technologies make it possible to obtain a product with a sufficiently high accuracy [16], but problems

arise in ensuring the stable quality of the density and structure of manufactured products with the use of finely dispersed powder metal materials [17]. A product with poor quality may be formed if the surface texture, particle sphericity and chemical composition of the powder of one batch differs. There are also disadvantages such as a low speed of manufacturing products [9] and a high risk of the formation of defects in the form of pores, which reduce the operational properties of products [18].

The technology of additive manufacturing by electric arc multilayer welding with a consumable electrode in a shielding gas environment is one of the least expensive and has high productivity. In the process of additive manufacturing products by the electric arc welding method, the wire is melted by the heat of the electric arc and the molten metal is transferred in drops to the weld pool. The heat source moves at the desired speed along a given trajectory. The molten metal of the weld pool crystallizes and forms a layer of the designed part [19]. Additive manufacturing allows the creation of a three-dimensional model in the metal layer by layer designed in a computer-aided design system [20–24]. Additive manufacturing by electric arc welding is currently gaining popularity in the aerospace industry, nuclear and chemical industries, mechanical engineering, shipbuilding and architecture [23]. Multilayer build-up welding of products by electric arc surfacing in an inert gas environment using a welding wire makes it possible to obtain a better uniform and dense deposited layer [24]. This is especially true because recently there has been a growing need for the manufacture of products with a geometry of varying complexity with minimal processing of the manufactured surface. However, this process has its drawbacks, among which are significant residual stresses due to overheating of the metal of the product [4,25]. An uneven distribution of heat over its volume occurs in the course of obtaining a product by multilayer build-up welding. In this regard, the accuracy of finished products obtained by the electric arc method is often lower than with the use of an electron or laser beam for multilayer build-up welding, but the speed of obtaining a deposited product is much higher. This is especially important when producing large parts in various industries [26].

In the manufacture of products using the method of multilayer build-up welding, metals with good weldability including steels [26–29], alloys based on Al [21,30], Ti [25,31–33] and Ni [34] can potentially be used. Martensitic and austenitic stainless steels are also successfully used for additive manufacturing of parts due to their outstanding mechanical properties and high corrosion resistance [35].

The effect of the thermal cycle of welding on the morphology, microstructure and mechanical properties of the additive manufacturing material occurs during the process of multilayer build-up welding of products by the method of electric arc welding. Significant influence is exerted by the amount of heat introduced, the cooling rate and the number of reheats of the product [11,36–40]. The use of limiters in the form of shaping blocks should contribute to the formation of the final pattern of heat distribution in the product, i.e., the structure and properties of the deposited material must change.

The purpose of this work is a comprehensive numerical and experimental study of the effect of side limiters (shaping blocks) on the formation of the structure of multilayer specimens made of stainless steel AISI 308LSi obtained by multilayer build-up welding.

2. Materials and Methods

The numerical simulation of the thermal pattern formation in the workpieces obtained by the method of build-up welding in a protective gas atmosphere was carried out using the finite element method. Figure 1 shows an isometric view of models of specimens obtained by multilayer build-up welding: 1—using heat-transfer limiters (shaping graphite blocks), then specimen №1; 2—using heat-removing limiters (shaping copper blocks), then specimen №2; 3—without limiters, then specimen №3.

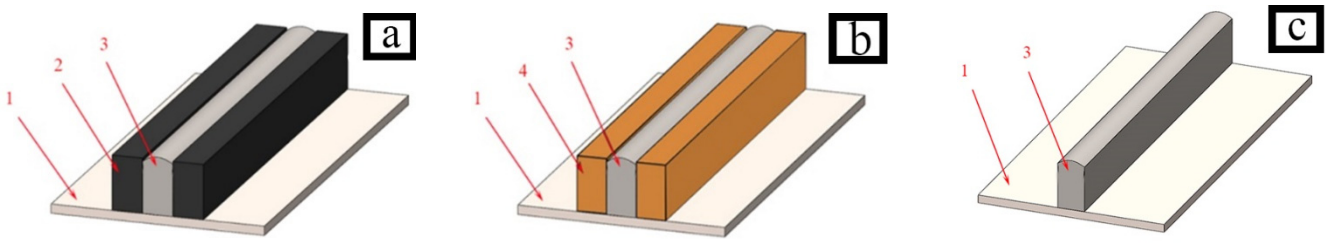

Figure 1. Isometric view of workpieces models obtained by multilayer build-up welding in a protective gas atmosphere: (**a**) using heat-transfer limiters (shaping graphite blocks); (**b**) using heat-removing limiters (shaping copper blocks); (**c**) without t limiters. 1—stainless steel substrate, 2—graphite shaping blocks (heat-transfer limiters), 3—build-up welded multilayer specimen, 4—copper shaping blocks (heat-removing limiters).

AISI 308LSi stainless steel wire was used for multilayer build-up welding of workpieces. This wire has a low carbon content and is designed for welding products used in a wide temperature range (−196 to 350 °C). Table 1 shows the chemical composition of the welding wire used [41].

Table 1. Chemical composition of AISI 308LSi welding wire.

C	Cr	Ni	Mn	Si	Mo	Other
max 0.03	19.9	10.5	1.8	0.9	0.15	Tot. <0.5

The properties of the AISI 308LSi steel material used are shown in Table 2 [41].

Table 2. Properties of steel AISI 308LSi.

Material	Melting Temperature T_{melt}, °C	Thermal Conductivity λ, W/m·K	Thermal Expansion Coefficient α, K^{-1}	Elastic Modulus E, GPa	Ultimate Strength σ_b, MPa	Yield Strength, MPa
AISI 308LSi	1450	12,642	16.5×10^{-6}	193	590	350

Figure 2 schematically shows a cross-sectional view of workpieces with the pointing of boundary conditions. The heat source for melting steel is shown in Figure 2 by a red arrow. Numerical simulation was carried out using 2D simplification to save time and computer resources. The boundary conditions have the form: $T|_{L2} = 1450$ °C, $u_x|_{L1} = 0$, $u_x|_{L3} = 0$, $u_y|_{L4} = 0$, where T is the applied temperature value, u_i is the displacement vector components. A mesh consisting of triangular finite elements was used in the numerical simulation.

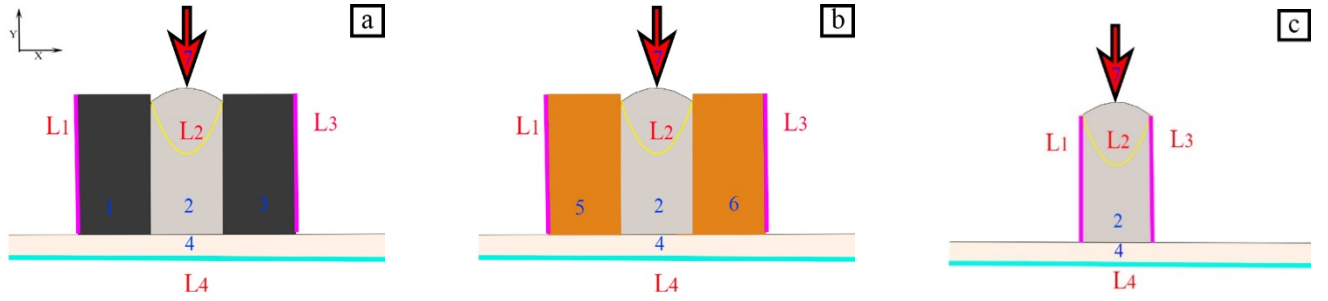

Figure 2. 2D cross-sectional view of modeled workpieces obtained by multilayer build-up welding with indication of elements and boundary conditions: (**a**) specimen №1; (**b**) specimen №2, (**c**) specimen №3. 1 and 3—heat-transfer limiters (shaping graphite blocks); 2—specimen;.4—substrate; 5 and 6—heat-removing limiters (shaping copper blocks); 7—heat source.

Multilayer workpieces were build-up by electric arc welding with consumable electrode AISI 308LSi with a diameter of 0.8 mm in argon, welding current I_{weld} = 100 A, arc voltage U = 20 V, gas consumption Q = 10 L/min, polarity reversed.

3. Numerical Simulation Results

Figure 3 shows the results of the numerical simulation of the thermal pattern formation of specimens of AISI 308LSi steel with multilayer build-up welding.

Analysis of the numerical simulation results (Figure 3) shows that with the use of the heat-transfer limiters, the maximum observed temperature in the specimen №1 is 1475 °C (under prescribed conditions). With the use of the copper (heat-removing) limiters, the maximum observed temperature in the specimen №2 decreased to 1450 °C (under prescribed conditions). This value is also equal to 1450 °C in the case of the build-up welding specimen №3 without the use of limiters. The temperature values along the axis of the specimens are noticeably different. Such a temperature difference is associated with the presence of blocks that provide different heat exchange with the environment.

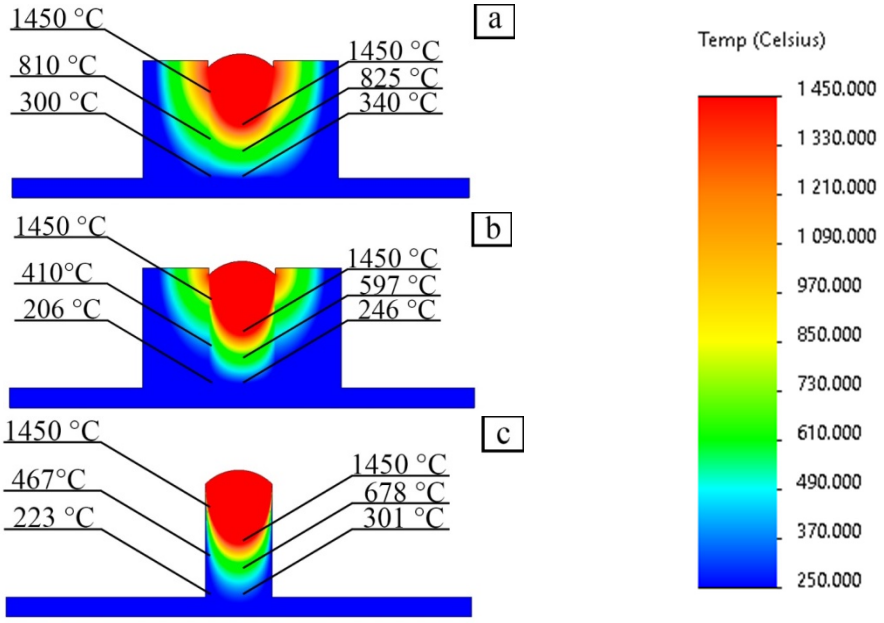

Figure 3. Results of simulation of the process of thermal pattern formation of AISI 308LSi steel workpieces obtained by multilayer build-up welding. Temperature values are given in °C. (**a**) specimen №1; (**b**) specimen №2, (**c**) specimen №3.

Figure 4 shows the cooling curve of stainless steel with a low carbon content (up to 0.03% mass). This curve allows us to better comprehend the processes taking place during multilayer build-up welding. The austenite phase (γ-Fe) is formed in the temperature range of 911…1499 °C and has higher hardness values compared to the ferrite phase (δ-Fe) by two-fold [42].

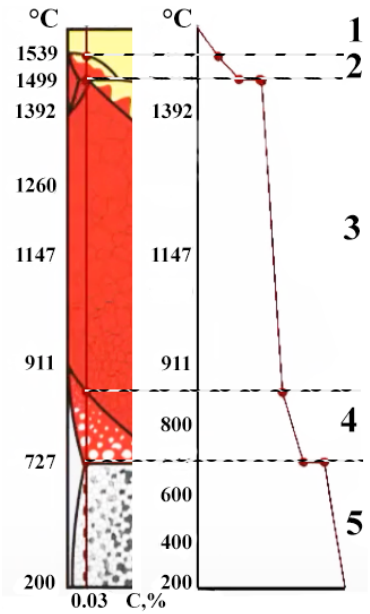

Figure 4. Cooling curve for steel with low carbon content (up to 0.03% mass): 1—there are no phase transformations, the liquid melt is cooled; 2—ferrite crystallization, the formation of δ-iron occurs, then in the region of 1499 °C the peritectic transformation δ-Fe + liquid phase → γ-Fe; 3—an γ-Fe phase is formed; 4—the formation of the γ-Fe + β-Ferrite phase occurs below a temperature of 911 °C; 5—the α-Ferrite+III Cementite phases is formed at temperatures below 727 °C.

Figure 5 presents the results of numerical modeling of the thermal pattern in the central and extreme lateral parts of the cross-sectional views of workpieces obtained under three different heat-transferring conditions. Areas are highlighted in color showing the proportion of workpiece material that is in the temperature range of the γ-Fe phase.

From Figure 5, it is found that the use of shaping graphite blocks has the greatest effect on the temperature increase both in the central and lateral parts of the cross-sectional view of specimen №1. Additionally, for the specimen №2, obtained using copper blocks, the lowest temperature value is observed in all parts of the specimen.

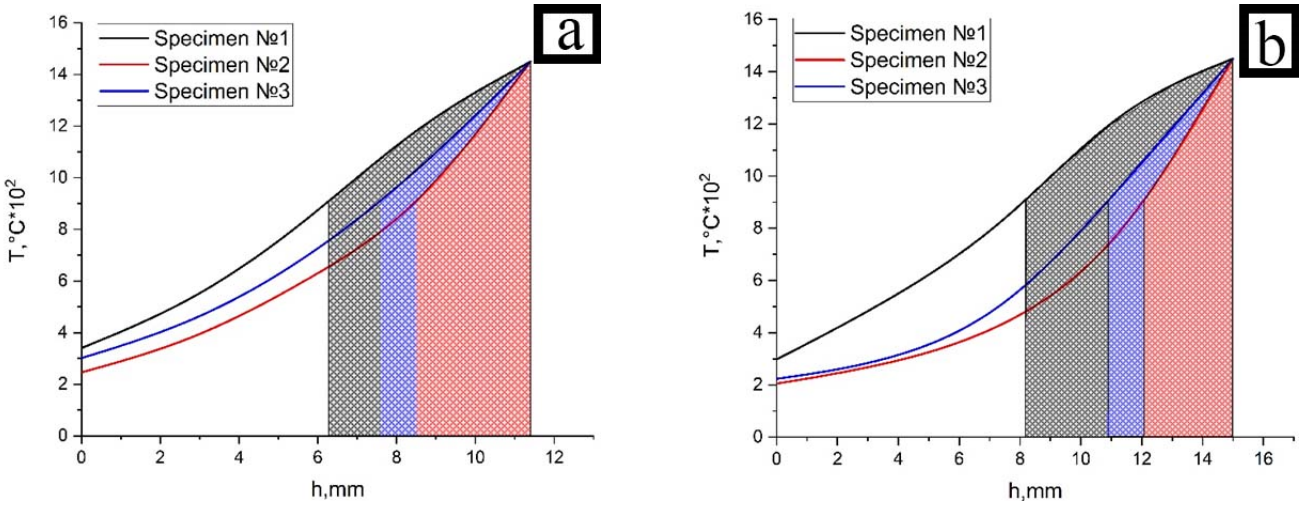

Figure 5. The results of numerical modeling the thermal pattern along the height of the cross-sectional view of workpieces: (**a**) in the central part; (**b**) at the extreme lateral part.

The proportion of material in the central part of specimen №1, which is in the temperature range of the formation of the γ-Fe phase, is 1.34 times greater than in specimen №3 obtained without the use of limiters, and 1.75 times greater than in the specimen №2. The difference in the proportions of metals between the specimens №2 and №3 is 24%.

A larger temperature difference occurs between the extreme lateral and central parts of specimen №2 with the use of copper blocks (Figure 5). This is due to the high thermal conductivity of copper. The opposite situation is observed in the case of using graphite blocks. A lower coefficient of thermal conductivity leads to a more uniform distribution of temperatures across the width of specimen №1. There is no difference in the proportions of metal in the temperature range of γ-Fe formation for specimen №1 (45% of the material in the central part, 45% of the material in the extreme lateral part). For specimen №2, this difference is 7% (26% in the central part, 19% in the extreme lateral part). For specimen №3, this difference is 6% (34% in the central part, 28% in the extreme lateral part). Thus, the use of shaping limiters in the form of graphite blocks has a significant effect on the formation of the workpiece structure and leads to an increase in the proportion of the γ-Fe phase by almost 1.5 times. Additionally, the use of copper blocks theoretically leads to a decrease in the proportion of the γ-Fe phase by almost 25%, in comparison with specimen № 3 without forming limiters.

The curves describing the thermal pattern formation in the central layers (Figure 5) were approximated by the least squares method. The resulting equation has the form y = mx + b, where m is the slope, and is also the first derivative of temperature with respect to time, which can be written as the rate of temperature change.

The temperature growth rate in the area of the central layers is $1.22 \times 10^2 \frac{^\circ C}{s}$ when the specimen №1 is obtained, which is 28% more than specimen №2, for which the temperature growth rate is $0.87 \times 10^2 \frac{^\circ C}{s}$. The temperature growth rate in the area of the central layers is $0.99 \times 10^2 \frac{^\circ C}{s}$ for the extreme lateral part of specimen №1, and for specimen №2 is $0.57 \times 10^2 \frac{^\circ C}{s}$, i.e., 42% more. The temperature growth rate in the central part of specimen №1 is 19% higher than the temperature growth rate at the extreme lateral part. For specimens №2 and №3, these relations are 34% and 24%, respectively. The above allows us to make an assumption about the uneven distribution of grain sizes in the case of copper blocks, and a more uniform distribution in the case of graphite blocks due to the difference between the patterns of heat distribution over the specimen.

Additionally, in Figure 5, slight changes in the behavior of the curve are observed at a temperature value of 911 °C for specimen №1. A decrease in the slope of the curve or the heating rate is observed after the inflection point (Figure 5a,b). This is due to increased heat removal from the upper surface of the specimen, since there is practically no heat removal from the lower surface due to the large volume of heated material in the central part.

4. Results and Discussion

Figure 6 shows images of specimens from cross-sections of workpieces obtained by multilayer build-up welding using AISI 308LSi welding wire in various heat transfer conditions.

From Figure 6, it can be observed that the use of shaping blocks (Figure 6a,b) makes it possible to obtain a final product with a flatter outside surface. The other side's unevenness projections are visible in case the specimen is obtained without the use of blocks (Figure 6c). The above makes it possible to further reduce the cost of mechanical post-processing by using the shaping blocks. In addition, the presence of symmetry should lead to a smaller difference between the property values in different parts of the build-up workpieces.

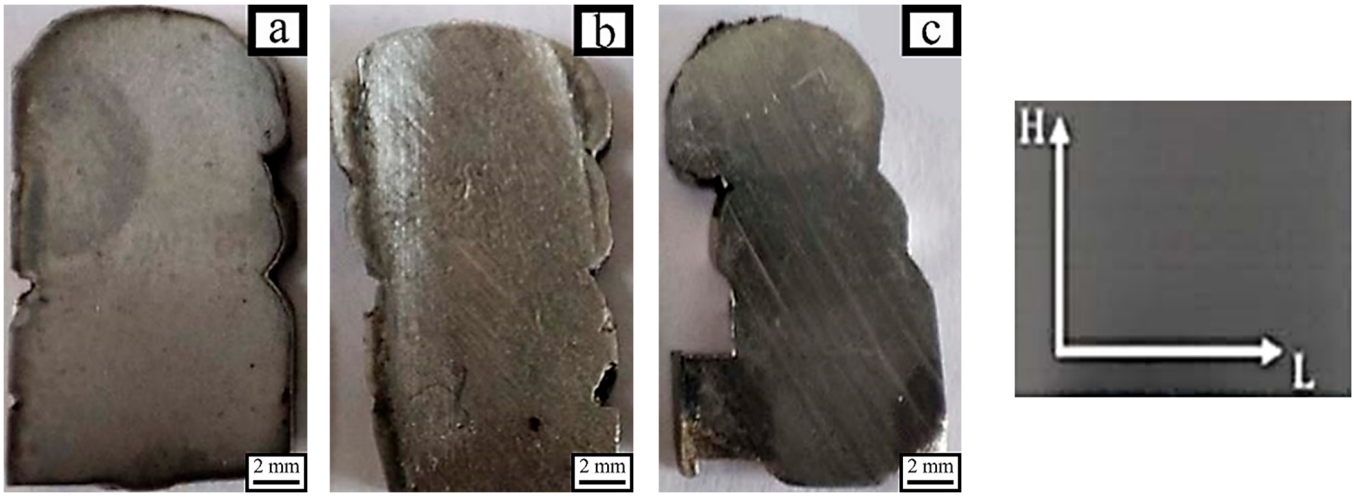

Figure 6. Images of specimens from cross-sections of investigated workpieces: (**a**) specimen №1; (**b**) specimen №2, (**c**) specimen №3.

For further investigation, dimensionless values for the height and width of the specimens were introduced due to the difference in sizes of workpieces (Figure 6). Specimen height (H) changes from 0 to h. The value of H = 0 corresponds to the transition area between the steel substrate and the first layer of the specimen. The width of the specimen (L) changes from 0 to l, where L = 0 corresponds to the left edge of the specimen, and L = l to the right edge. The geometric parameters of the specimens were divided into equal parts: 0.25; 0.5; 0.75; and 1. Figure 7 shows bright-field images of structures along the axis (L = l/2) of the cross-sections of the investigated specimens.

In specimen №3, clear junction regions between layers are observed (Figure 7m,o). These regions are accompanied by broadening of the dendrites up to the upper part of the specimen. The presence transition areas are associated with increased heat-removal from all sides of the specimen. A strict orientation of the dendrites along the height of the specimen is also observed. It should be noted that transition area between the substrate and the first deposited layer is also observed. This area is represented by large grains of the steel substrate which travel to dendrites of the first build-up welded layer.

The transition area between the steel substrate and the deposited material is also clearly visible in specimen №2. However, the size of the dendrites is smaller compared to specimen №3. This is due to the high value of the thermal conductivity of copper, as a result of which the crystallization process occurs faster. The transition zones are not so clearly visible, and their width is ~80μm in the central parts of the specimen (Figure 7g).

In turn, for specimen № 1, a smooth transition between layers is observed. The presence of graphite blocks leads to the retention of heat in the area between them. As a result, heat is redistributed in the volume of the workpiece and sharp transitions between layers are not formed. Additionally, in the area between the steel substrate and the first layer a smoother transition is observed unlike other samples. The above suggests that the values of mechanical properties in different parts of the specimen №1 will practically not differ. Figure 8 shows the dendritic thickness value distribution along the height of the specimens in the regions L = l/2 (Figure 8a) and L = 0 (Figure 8b).

Figure 8 shows that the dendritic thickness in specimen №1 is greater on 1.6 times compared with specimen №3, both in the central and in the extreme lateral part. This relation between specimens №1 and №2 is 2.5 times in the central part and 3.5 times in the extreme lateral part. The pattern of the distribution of the values of dendritic thickness for specimen №1 is retained in contrast to specimens №2 and №3. Inflections on the curve for specimens № 2 and №3 show the uneven distribution of heat in the metal. These data correlate well with the above simulation results. The obtained dependencies were approximated by the least squares method. The growth rate of dendrites is 18.3 $\frac{\mu m}{s}$ in

specimen №1. This is 1.5 times more in the case of specimen №3, for which the dendrite growth rate is 12.1 $\frac{\mu m}{s}$, and 3.2 times more compared to specimen №2, for which the growth rate of dendrites is 5.7 $\frac{\mu m}{s}$. The lowest value of the dendrite growth rate for specimen №2 is determined by the large value of the thermal conductivity coefficient in comparison with specimens №1 and №3, for which the heat exchange between the specimen metal and the environment proceeded more slowly and more favorable conditions arose for the growth of dendrites.

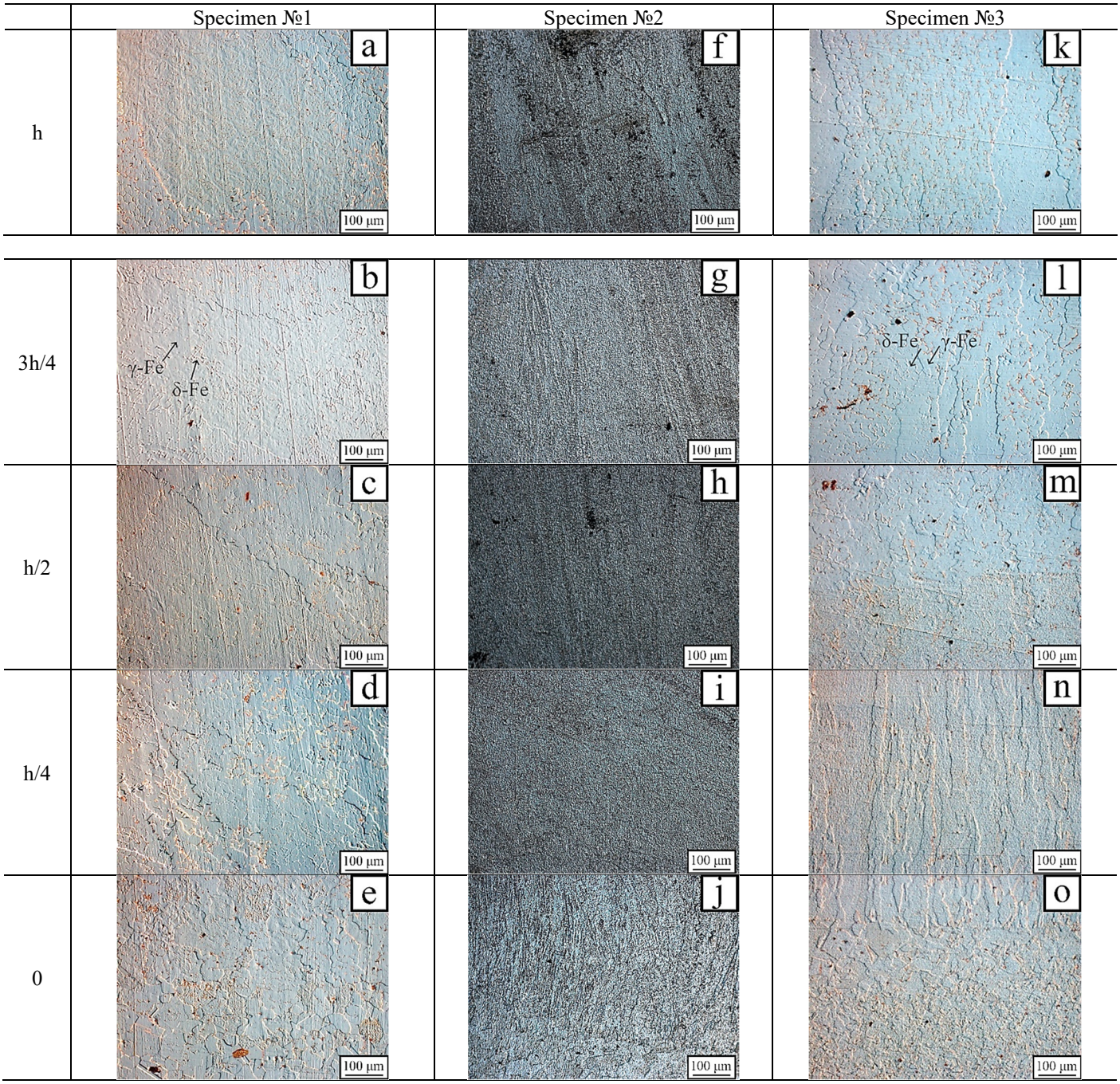

Figure 7. Bright-field images of structures along the axis (L = l/2) of cross-sections of specimens: (**a**–**e**)—specimen №1, (**f**–**j**)—specimen №2, (**k**–**o**)—specimen №3.

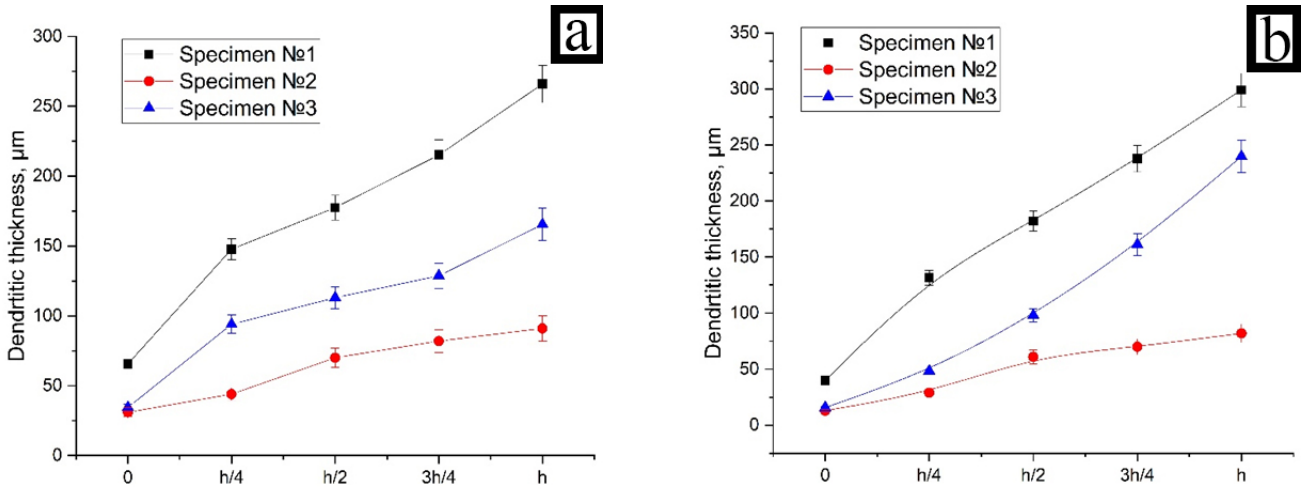

Figure 8. Distributions of dendritic thickness values in height: (**a**) in the central part; (**b**) in the extreme lateral part.

The relative deviations of the dendritic thickness were calculated by the equation:

$$\delta_H = \frac{d_{cH} - d_{elH}}{d_{elH}} * 100\% \quad (1)$$

where δ_H = value of the relative deviation at a certain H point, d_{cH} = value of the dendritic thickness in the central part at a certain H point, value of the dendritic thickness in the extreme lateral part at a certain H point.

The values of the dendritic thickness relative deviations in the central and extreme lateral parts are shown in Figure 9.

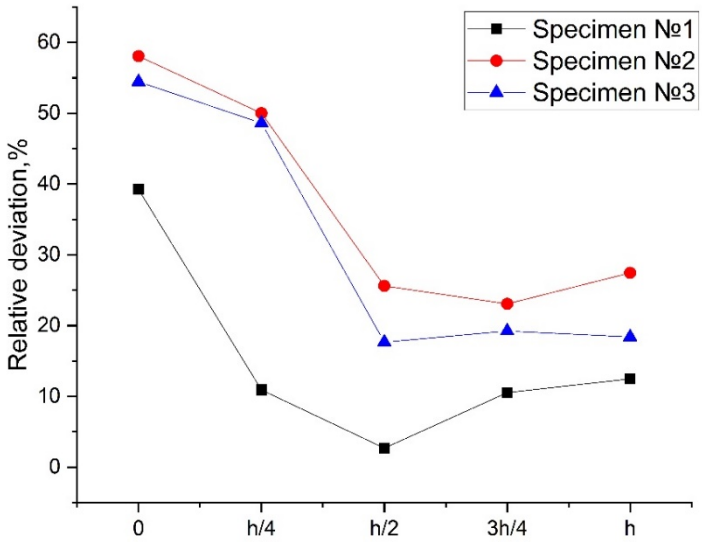

Figure 9. Dependencies of the values of the dendritic thickness relative deviation along the height of the specimens.

As shown in Figure 9, it was found that for all three specimens there is a tendency to decrease in the relative deviation of the values of the dendritic thickness in the central region of the specimens and an increase in the lower and upper parts of the specimens. However, for specimen №1, the deviation value in the central part is 2.6%, in contrast to specimen №3, for which this value is 17%. The highest value of the relative deviation equal to 23% is observed for specimen №2. The results obtained confirm the assumptions made

from the results of numerical simulation that the most uniform distribution of dendrites sizes is observed for specimen № 1. Graphite blocks do not allow the specimen to actively release heat into the environment unlike copper blocks, which in this case played the role of heat exchangers.

Dependences of the change in the dendritic thickness on temperature in the central part of the cross-section of the specimens were obtained (Figure 10) based on the analysis of the investigation results (Figures 5 and 8).

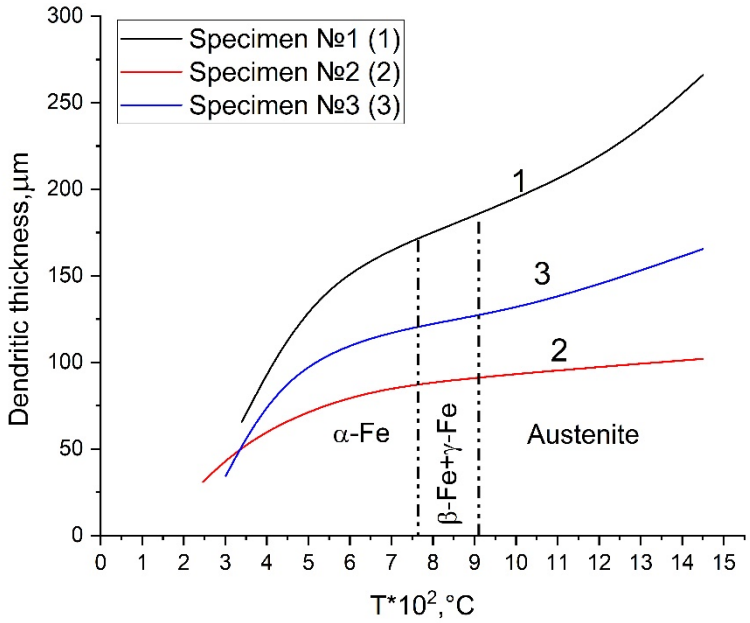

Figure 10. Dependences of the dendritic thickness from temperature in the central part of the cross-section of the specimens.

As shown in Figure 10, it was found that most of the curve for specimen №1 is located in the temperature region of the γ-Fe phase. Increasing the temperature above 911 °C leads to the formation of an γ-Fe phase. The area of regions containing the austenite phase for specimens №1 and №3 is 61% and 54%, respectively. For specimen №2, this value is 58%. Thus, specimen №1 should have a smaller content of δ-Fe phase than specimens №2 and № 3. The above phase transformations can lead to an increase in the mechanical properties of build-up welded workpieces. It is due to the hardness of austenite, which is about 2 times greater than then of ferrite [42]. The hardness of the three specimens was measured to confirm this assumption.

Figure 11 shows the changes in hardness in the cross-sections of specimens №1, №2 and №3 along the height in the regions L = l/2 (Figure 11a) and L = 0 (Figure 11b).

From Figure 11a,b, it can be seen that the hardness of specimen №1 is higher. The hardness increase is 10% and 12% in all investigated areas compared to specimens №2 and №3, respectively. The pattern of the distribution of hardness values in the central parts of the specimens is similar. There is a slight decrease in hardness caused by the factor of increasing the size of the structural elements. The hardness begins to be influenced by the factor of austenite content in the bulk of the material further along the height of the specimen. In this regard, there is a distinct peak in the central part for specimen №1. It should be noted that specimen №2 has a higher hardness compared to specimen №3 on average by 5%. The hardness value is affected by the small size of the dendrites in specimen №2 in this case. The proportion of the austenite phase in specimen №3 is not enough to compensate for the effect of the size of the dendrites. The proportion of austenite decreases with the move from the central parts of the specimens to the upper part, which leads to a slight decrease in the hardness of the specimens. The inflections observed at point H = h/2

can be explained by the uneven pattern of the heat distribution in the central part of the specimens. Due to this an area with an increased hardness is formed.

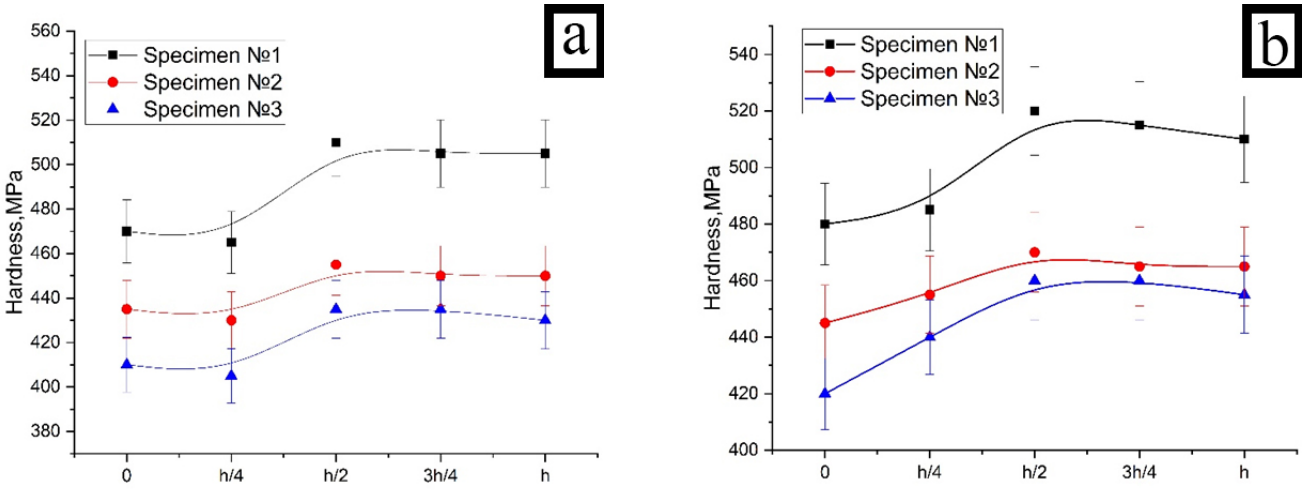

Figure 11. Distribution of hardness values along the height of the cross-section of the specimens: (**a**) in the central part; (**b**) in the extreme lateral part.

The dependencies of relative deviations of hardness values of the central and extreme lateral parts of the specimens are shown in Figure 12.

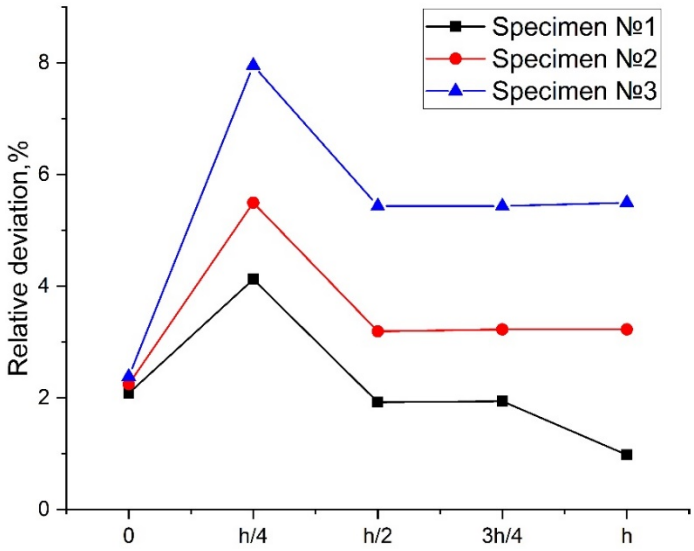

Figure 12. Dependencies of relative deviation of the hardness values along the height of the specimens.

As shown in Figure 12, it was found that for all three specimens, there is a tendency to an abrupt increase in the relative deviation of the hardness values in the region of the first layer of the specimens. This is due to the fact that in all three cases under the action of heat removal from the side of the substrate, the properties are distributed more uniformly over the width of the specimens than in the transition region between the first and second layers of the specimens, where a higher temperature is maintained in the center of the specimen compared to the lateral part. The above is confirmed by the previously presented results of numerical simulation. The values of the relative deviations decrease, and the dependences become linear further up the height of the specimens. The exception is specimen №1, for which there is a decrease in the value of the relative deviation in the upper layer. This decrease is caused by a small difference between the temperatures in the central and lateral parts due to the low rate of heat removal from the graphite blocks. For specimen №1, the

deviation values range from 1 to 4%, unlike specimens № 2 and № 3, for which these values vary in the range from 2 to 5% and from 2 to 7%, respectively.

Thus, the use of heat-transfer limiters in the form of graphite blocks makes it possible to obtain a finished product with a more uniform distribution of structure and properties over the volume of the deposited metal of the specimen. This allows a better prediction to made of the behavior of the material under the influence of various loads by creating a mathematical model based on the experimental data obtained. The greater deviation of the hardness values in width for specimen №3 is associated with phase transformations during heat transfer with the environment. During this time, the proportion of the ferrite phase prevails at the edges of the specimen compared to specimen № 1, as well as the large size of dendrites compared to specimen №2. Not only the phase composition but also the elements sizes of the formed structure play a significant role in the formation of material properties during crystallization. The use of copper blocks leads to the formation of a structure that is smaller in size, i.e., in the case of using other materials for build-up welding can be a plus. Recommendations will be developed for obtaining high-quality stainless-steel products with a carbon content of up to 0.03% multilayer build-up welding in a protective gas environment based on the results obtained.

5. Conclusions

The positive effect of the use of shaping blocks in multilayer build-up welding in a protective gas environment has been established:

1. They make it possible to reduce the cost of machining due to their ability to produce workpieces with flat side surfaces.
2. The use of graphite blocks makes it possible to form the structure of the AISI 308LSi stainless-steel workpiece with smooth transitions between the build-up welded layers. There is an increase in the hardness value due to the more active diffusion of δ-ferrite into γ-Fe by an average of 12% compared with the studied specimens despite the overall increase in the size of dendrites. The technology of multilayer build-up welding makes it possible to produce a workpiece with a homogeneous distribution of structure and properties. The above makes them a promising direction in electric arc additive manufacturing.
3. The use of copper blocks leads to the formation of a specimen metal structure that is smaller in size but has lower hardness compared to a specimen obtained using graphite blocks.

Author Contributions: Conceptualization, methodology, writing—review and editing: D.A.C. and K.O.A.; sample preparation, supervision: D.A.C.; data processing, investigation: K.O.A. All authors have read and agreed to the published version of the manuscript.

Funding: The work was performed according to the Government research assignment for ISPMS SB RAS, project FWRW-2021-0003.

Institutional Review Board Statement: Not applicable.

Informed Consent Statement: Not applicable.

Data Availability Statement: Not applicable.

Conflicts of Interest: The authors declare no conflict of interest.

References

1. Wohlers, T. *Additive Manufacturing and 3D-Printing State of the Industry: Annual Worldwide Progress Report*; Wohlers Associates: Fort Collins, CO, USA, 2014; p. 276.
2. *ASTM F2792-12a*; Standard Terminology for Additive Manufacturing Technologies. ASTM International: West Conshohocken, PA, USA, 2015.
3. Kuznetsov, M.A.; Danilov, V.I.; Krampit, M.A.; Chinakhov, D.A.; Slobodyan, M.S. Mechanical and tribological properties of a metal wall grown by an electric arc method in an atmosphere of shielding gas. *Met. Work. Mater. Sci.* **2020**, *22*, 18–32. [CrossRef]
4. Yan, X.; Gu, P. A review of rapid prototyping technologies and systems. *Comput. Aided Des.* **1996**, *28*, 307–318. [CrossRef]

5. Gisario, A.; Kazarian, M.; Martina, F.; Mehrpouya, M. Metal additive manufacturing in the commercial aviation industry: A review. *J. Manuf. Syst.* **2019**, *53*, 124–149. [CrossRef]
6. *DIN EN ISO/ASTM 52900:2018*; Additive Manufacturing; Deutsche und Englische Fassung prEN_ISO/ASTM 52900:2018. Beuth Verlag: Berlin, Germany, 2018.
7. Murr, L.E.; Gaytan, S.M.; Ramirez, D.A.; Martine, E.; Hernandez, J.; Amato, K.N.; Shindo, P.W.; Medina, F.R.; Wicker, R.B. Metal fabrication by additive manufacturing using laser and electron beam melting technologies. *J. Mater. Sci. Technol.* **2012**, *28*, 1–14. [CrossRef]
8. Gu, D.D.; Meiners, W.; Wissenbach, K.; Poprawe, R. Laser additive manufacturing of metallic components: Materials, processes and mechanisms. *Int. Mater. Rev.* **2012**, *57*, 133–164. [CrossRef]
9. Sing, S.L.; An, J.; Yeong, W.Y.; Wiria, F.E. Laser and electron-beam powder-bed additive manufacturing of metallic implants: A review on processes, materials and designs. *J. Orthop. Res.* **2016**, *34*, 369–385. [CrossRef] [PubMed]
10. Queguineur, A.; Rückert, G.; Cortial, F.; Hascoët, J.Y. Evaluation of wire arc additive manufacturing for large-sized components in naval applications. *Weld. World* **2018**, *62*, 259–266. [CrossRef]
11. Rodriguez, N.; Vázquez, L.; Huarte, I.; Arruti, E.; Tabernero, I.; Alvarez, P. Wire and arc additive manufacturing: A comparison between CMT and Top TIG processes applied to stainless steel. *Weld. World* **2018**, *62*, 1083–1096. [CrossRef]
12. Bekker AC, M.; Verlinden, J.C. Life cycle assessment of wire + arc additive manufacturing compared to green sand casting and CNC milling in stainless steel. *J. Clean. Prod.* **2018**, *177*, 438–447. [CrossRef]
13. Elmer, J.W.; Gibbs, G. The effect of atmosphere on the composition of wire arc additive manufactured metal components. *Sci. Technol. Weld. Join.* **2019**, *24*, 367–374. [CrossRef]
14. Lu, T.; Liu, C.; Li, Z.; Wu, Q.; Wang, J.; Xu, T.; Liu, J.; Wang, H.; Ma, S. Hot-wire arc additive manufacturing Ti-6.5Al-2Zr-1Mo-1V titanium alloy: Pore characterization, microstructural evolution, and mechanical properties. *J. Alloys Compd.* **2020**, *817*, 153334. [CrossRef]
15. Zhang, Q.; Zhang, B.; Luo, Y.; Yang, G.; Zheng, H.-X. Effect of the welding process on microstructure, microhardness, and residual stresses of capacitor discharge stud welded joint. *J. Manuf. Sci. Eng.* **2022**, *144*, 011007. [CrossRef]
16. Zhai, Y.; Lados, D.A.; LaGoy, J.L. Additive Manufacturing: Making Imagination the Major Limitation. *JOM* **2014**, *66*, 808–816. [CrossRef]
17. Strondl, A.; Lyckfeldt, O.; Brodin, H.; Ackelid, U. Characterization and control of powder properties for additive manufacturing. *JOM* **2015**, *67*, 549–554. [CrossRef]
18. Slotwinski, J.A.; Garboczi, E.J.; Stutzman, P.E.; Ferraris, C.F.; Watson, S.S.; Peltz, M.A. Characterization of metal powders used for additive manufacturing. *J. Res. Natl. Inst. Stand. Technol.* **2014**, *119*, 460. [CrossRef]
19. Khairallah, S.A.; Anderson, A.T.; Rubenchik, A.; King, W.E. Laser powder-bed fusion additive manufacturing: Physics of complex melt flow and formation mechanisms of pores, spatter, and denudation zones. *Acta Mater.* **2016**, *108*, 36–45. [CrossRef]
20. Khadyko, M.; Marioara, C.D.; Ringdalen, I.G.; Dumoulin, S.; Hopperstad, O.S. Deformation and strain localization in polycrystals with plastically heterogeneous grains. *Int. J. Plast.* **2016**, *86*, 128–150. [CrossRef]
21. Guo, N.; Leu, C. Additive manufacturing: Technology, applications and research needs. *Front. Mech. Eng.* **2013**, *8*, 215–243. [CrossRef]
22. Gu, J.; Ding, J.; Williams, S.W.; Gu, H.; Bai, J.; Zhai, Y.; Ma, P. The strengthening effect of inter-layer cold working and post-deposition heat treatment on the additively manufactured Al–6.3 Cu Alloy. *Mater. Sci. Eng. A* **2016**, *651*, 18–26. [CrossRef]
23. Li, R.; Xiong, J.; Lei, Y. Investigation on thermal stress evolution induced by wire and arc additive manufacturing for circular thin-walled parts. *J. Manuf. Process.* **2019**, *40*, 59–67. [CrossRef]
24. Murr, L.E.; Gaytan, S.; Ceylan, A.; Martinez, E.; Martinez, J.; Hernandez, D.; Machado, B.I.; Ramirez, D.A.; Medina, F.; Collins, S.; et al. Characterization of titanium aluminide alloy components fabricated by additive manufacturing using electron beam melting. *Acta Mater.* **2010**, *58*, 1887–1894. [CrossRef]
25. Williams, S.W.; Martina, F.; Addison, A.C.; Ding, J.; Pardal, G. Colegrove Wire+ arc additive manufacturing. *Mater. Sci. Technol.* **2016**, *32*, 641–647. [CrossRef]
26. Wu, B.; Pan, Z.; Ding, D.; Cuiuri, D.; Li, H.; Xu, J.; Norrish, J. A review of the wire arc additive manufacturing of metals: Properties, defects and quality improvement. *J. Manuf. Process.* **2018**, *35*, 127–139. [CrossRef]
27. Karayel, E.; Bozkurt, Y. Additive manufacturing method and different welding applications. *J. Mater. Res. Technol.* **2020**, *9*, 11424–11438. [CrossRef]
28. Luo, Y.; Gu, W.; Peng, W.; Jin, Q.; Qin, Q.; Yi, C. A Study on Microstructure, Residual Stresses and Stress Corrosion Cracking of Repair Welding on 304 Stainless Steel: Part I-Effects of Heat Input. *Materials* **2020**, *13*, 2416. [CrossRef] [PubMed]
29. Hu, X.; Jiang, H.-Y.; Luo, Y.; Gin, Q.; Peng, W.; Yi, C.-M. A Study on Microstructure, Residual Stresses and Stress Corrosion Cracking of Repair Welding on 304 Stainless Steel: Part II-Effects of Reinforcement Height. *Materials* **2020**, *13*, 2434. [CrossRef]
30. Yan, L. Wire and Arc Addictive Manufacture (WAAM) Reusable Tooling Investigation. 2013. Available online: https://dspace.lib.cranfield.ac.uk/handle/1826/12308 (accessed on 23 February 2020).
31. Brice, C.; Shenoy, R.; Kral, M.; Buchannan, K. Precipitation behavior of aluminum alloy 2139 fabricated using additive manufacturing. *Mater. Sci. Eng. A* **2015**, *648*, 9–14. [CrossRef]
32. Leyens, C.; Peters, M. *Titanium and Titanium Alloys: Fundamentals and Applications*; John Wiley & Sons: Hoboken, NJ, USA, 2003.

33. Kim, T.B.; Yue, S.; Zhang, Z.; Jones, E.; Jones, J.R.; Lee, P. Additive manufactured porous titanium structures: Through-process quantification of pore and strut networks. *J. Mater. Process. Technol.* **2014**, *214*, 2706–2715. [CrossRef]
34. Xu, F.; Lv, Y.; Liu, Y.; Shu, F.; He, P.; Xu, B. Microstructural Evolution and Mechanical Properties of Inconel 625 Alloy during Pulsed Plasma Arc Deposition Process. *J. Mater. Sci. Technol.* **2013**, *29*, 480–488. [CrossRef]
35. Bressan, J.; Daros, D.; Sokolowski, A.; Mesquita, R.; Barbosa, C. Influence of hardness on the wear resistance of 17-4 PH stainless steel evaluated by the pin-on-disc testing. *J. Tianmater. Process. Technol.* **2008**, *205*, 353–359. [CrossRef]
36. Chen, X.; Li, J.; Cheng, X.; He, B.; Wang, H.; Huang, Z. Microstructure and mechanical properties of the austenitic stainless steel 316L fabricated by gas metal arc additive manufacturing. *Mater. Sci. Eng. A* **2017**, *703*, 567–577. [CrossRef]
37. Yadollahi, A.; Shamsaei, N.; Thompson, S.M.; Seely, D.W. Effects of process time interval and heat treatment on the mechanical and microstructural properties of direct laser deposited 316L stainless steel. *Mater. Sci. Eng. A* **2015**, *644*, 171–183. [CrossRef]
38. Stützer, J.; Totzauer, T.; Wittig, B.; Zinke, M.; Jüttner, S. GMAW Cold Wire Technology for Adjusting the Ferrite–Austenite Ratio of Wire and Arc Additive Manufactured Duplex Stainless Steel Components. *Metals* **2019**, *9*, 564. [CrossRef]
39. Wang, L.; Xue, J.; Wang, Q. Correlation between arc mode, microstructure, and mechanical properties during wire arc additive manufacturing of 316L stainless steel. *Mater. Sci. Eng. A* **2019**, *751*, 183–190. [CrossRef]
40. Jiang, W.; Luo, Y.; Deng, Y.; Wan, Y.; Chen, J. Effect of Cooling Rate on Phase Transformation and Strain Response of SA508-3 Steel by Numerical and Experimental Study. *J. Press. Vessel. Technol.* **2022**, *144*, 061501. [CrossRef]
41. Stainless Steel Technical Handbook. ESAB [Electronic Resource]. Available online: https://www.alas-kuul.ee/media/wysiwyg/CMS/Stainless%20handbook.pdf (accessed on 9 July 2021).
42. Zimmermann, R.; Günther, K. *Metallurgie und Werkstofftechnil: Ein Wissensspeicher*; Deutscher Verlag für Grundstoffindustrie: Leipzig, Germany, 1977; p. 679.